Journal of Petroleum Science and Engineering 208 (2022) 109334

Contents lists available at ScienceDirect

Journal of Petroleum Science and Engineering

journal homepage: www.elsevier.com/locate/petrol

Cement properties characterization from a section retrieved from an oil production well after 33 years of downhole exposure

Katherine Beltrán-Jiménez [a,b,e,*], Dave Gardner [a], Steinar Kragset [a], Kidane F. Gebremariam [d], Oscar A.M. Reales [e], Mona W. Minde [c], Marcelo I.L. de Souza [e], Jan A. Aasen [b], Hans J. Skadsem [a,b], Laurent Delabroy [f]

[a] NORCE Norwegian Research Centre, Olav Hanssensvei 15, 4021, Stavanger, Norway
[b] Department of Energy and Petroleum Engineering, Universitetet i Stavanger, Kjell Arholms gate 41, 4036 Stavanger, Norway
[c] Department of Mechanical Engineering, Construction and Materials Technology, Universitetet i Stavanger, Kjell Arholms gate 41, 4036 Stavanger, Norway
[d] Archeological Museum, Department of Conservation, Universitetet i Stavanger, Kjell Arholms gate 41, 4036 Stavanger, Norway
[e] Federal University of Rio de Janeiro, Cidade Universitária, Ilha do Fundão, Brazil
[f] Aker BP ASA, Jattavagveien 10, 4020, Stavanger, Norway

ARTICLE INFO

Keywords:
Plug & abandonment
Cement characterization
Cement durability
Well integrity

ABSTRACT

A unique data set has been constructed based on the study of class G cement recovered from an oil well on the Norwegian continental shelf. The cement was placed between two casing sections and submitted to downhole conditions for 33 years. The aim of this research is to analyze the aging of the cement and its consequences for the well integrity. Additionally, the findings represent a baseline for future assessments of old age cement from oil and gas wells. The characterization includes: petrophysical properties (porosity and permeability); mechanical properties (uniaxial compressive strength (UCS) and Young's Modulus); and compositional analysis using Computed Tomography (CT), Scanning Electron Microscopy (SEM), X-ray Fluorescence (XRF) and Quantitative X-ray Diffraction (XRD). Findings suggest that the overall decrease of cement integrity appears to be low, since the magnitudes of permeability and porosity fall within the ranges of early age cement. However, the chemical characterization shows that mud contamination may have an effect on the cement performance and is found to be relevant for a reduction in compressive strength.

1. Introduction

Cement is the most important material used to construct barriers nowadays, not only for oil and gas wells, but also for geothermal wells (Shadravan and Shine, 2015; Lohne et al., 2016) and underground CO_2 storage facilities (Carey et al., 2007). In the oil industry, during well construction, cement is pumped into annular spaces to obtain well integrity, provide zonal isolation along the annulus, maintain mechanical support and prevent communication between the surroundings and the well fluids. During cement placement, operative conditions can compromise the zonal isolation due to incomplete drilling fluid displacement resulting in voids, channels and slurry contamination (Hart and Smith, 1990; Guillot et al., 2008a; Chen et al., 2014; Skadsem et al., 2019).

After placement and throughout the well life cycle, cement is normally exposed to gases and fluids from different sources. It is also subject to changes in pressure and temperature. These could negatively affect the cement properties with adverse consequences concerning its effectiveness as a barrier in a long-term perspective. The recognized factors that potentially affect the cement properties include: water penetration, gas migration, chemical attack and variations in pressure and temperature that are able to generate thermo-mechanical failures such as shrinkage, cracking and debonding (Kiran et al., 2017; Andrade et al., 2016; Ferreira et al., 2019). Mapping the consequence of these factors with a long-term perspective is a challenging and complex task but three main processes are identified as the most critical: increases in porosity and permeability, reduction of mechanical resistance and the creation of fluid migration paths that can allow the migration of fluids through a barrier creating well integrity problems such as Sustained Casing Pressure (SCP) (Bourgoyne et al., 1999; Wojtanowicz et al., 2001).

The cement properties for early age cement have been extensively investigated in the laboratory, see e.g. Justnes et al. (1995). However, studies related to durability are sparse but the recent increased interest in projects for Carbon Capture and Storage (CCS) have improved the

* Corresponding author at: NORCE Norwegian Research Centre, Olav Hanssensvei 15, 4021, Stavanger, Norway.
E-mail address: kaji@norceresearch.no (K. Beltrán-Jiménez).

https://doi.org/10.1016/j.petrol.2021.109334
Received 4 May 2021; Received in revised form 12 July 2021; Accepted 3 August 2021
Available online 8 August 2021

understanding of cement degradation mechanisms such as carbonation and bicarbonation occurring when CO_2 reacts with cement. As a consequence, the degradation due to CO_2 exposure is nowadays relatively well understood based on contributions from different researchers who have analyzed the changes in cement properties, phases and microstructure in the laboratory (Agbasimalo and Radonjic, 2012; Duguid et al., 2005; Duguid, 2009; Duguid and Scherer, 2010; Raoof et al., 2012; Lécolier et al., 2007; Wolterbeek et al., 2016). Degradation due to H_2S exposure and brine penetration have been less studied but a few authors have published some findings from laboratory experiments concluding that leaching and calcium loss are the main degradation mechanisms (Noik and Rivereau, 1999; Buzzi et al., 2007; Xie et al., 2008; Garnier et al., 2012; Vrålstad et al., 2016). The studies of hydrocarbon penetration for aging and reaction with cement have been sparse and the results did not show alterations in the mechanical properties (Lécolier et al., 2007; Vrålstad et al., 2016).

The studies of durability of cement recovered from oil wells after exposure to downhole conditions are limited. The effects of degradation on oil field recovered samples were studied by Duguid et al. (2013) and Scherer et al. (2011) with analysis limited to petrophysical properties and SEM. A few studies present the results of the combined effect of aging and degradation due to exposure to CO_2 (Carey et al., 2007; Crow et al., 2010). In this context, the present work is a pioneer study of cement slurry characterization after 33 years of exposure to downhole well conditions. In the following sections an in-depth characterization (including petrophysical, mechanical properties and compositional analysis) of class G cement samples recovered from an offshore wellbore system is presented. The results provide a unique opportunity to establish a baseline to assess the effect of aging on cement properties and composition, whereas most of the previous studies of cement durability for field samples combine the effects of aging and CO_2 exposure making it difficult to address the alteration due to age effects alone.

2. Field and well background

The Valhall field is located in the southern part of the Norwegian sector of the North Sea, approximately 290 km offshore and in 69 m water depth. The presence of exploitable hydrocarbons was discovered in 1975 and the field started production in 1982 from an over pressured, under-saturated Upper Cretaceous chalk reservoir (Munns, 1985). The field produces paraffinic oil of 36 API gravity from the Tor and Lower Hod formations, producing 500 MMSTB (79.5×10^6 m^3) by 2002 (Barkved et al., 2003) and doubling this volume by 2017, when a production record of 1000 MMSTB (159×10^6 m^3) was achieved. Currently, the field consists of six platforms and has simultaneous activities including production, drilling operations and plug and abandonment (P&A) (AkerBP, 2018).

Up to now, 14 wells have been permanently P&A'd on the Valhall field, in accordance with the requirements of the Petroleum Safety Authority (PSA) ("Petroleum Safety Authority of Norway Regulations", 2014, 2018) and the guideline NORSOK D-010 ("Standards Norway", 2013). When it comes to meeting the national requirements, what has proven challenging and time consuming is the removal of casing sections in the upper part of the wells, in order to place cross-sectional surface barriers. This procedure is required for wells recorded to have Sustained Casing Pressure (SCP) records and/or poor cement quality behind the casing.

One well originally drilled and completed in 1985 and in production for 33 years was submitted to well integrity assessment prior to the abandonment operation. Cement evaluation was performed using acoustic logging tools which indicated poor bond quality in the upper interval and moderate to poor quality in the lower intervals (Palacio et al., 2020). The well records showed 50 bar of SCP and $CaBr_2$ brine trapped and stationary for more than 2 years in the annulus between the 9 5/8" (0.244 m) and 13 3/8" (0.339 m) casing. Based on the log

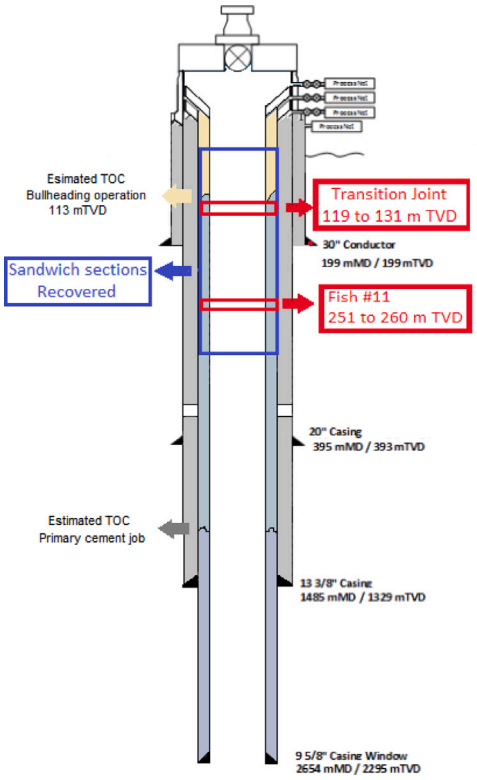

Fig. 1. Well design showing the location of sections. In purple the twenty three recovered sections and in red the two sections, our object of study.

assessment, the operator chose to cut and recover sections of 13 3/8" and 9 5/8" casing strings with class G cement in between. Additional details describing the well logging, retrieval operation and surface re-logging are presented in Palacio et al. (2020). In total, twenty-six sandwich sections were recovered (over the interval 47 to 376 m well depth) enabling the subsequent installation of the surface barrier between 138 and 222 m. The location in the well from which the sandwich sections were recovered is shown in Fig. 1.

The well reports were consulted to better understand the cement contained in the sections. The 13 3/8" casing section was cemented to surface with 100% returns, whereas the 9 5/8" casing was cemented in two stages. The first stage was a conventional job whereby the cement slurries were displaced down the inside of the casing and up into the annulus. Two slurries were pumped in this stage: A lead slurry with 15.5 ppg (1857 kg m^{-3}) density and a tail slurry with 15.8 ppg (1893 kg m^{-3}). The liquid phase was prepared with drill water including additives for fluid loss control. The estimated W/C ratios were 0.48 and 0.45 for the lead and tail slurries. The first stage resulted in a cement job without returns to surface due to the losses to a weak formation, so a second cement job was performed by bullheading cement through the annulus from surface. For this slurry, the liquid phase was prepared with sea water and the W/C ratio was 0.45, the slurry had 15.8 ppg (1893 kg m^{-3}).

Two of the twenty-six recovered sandwich sections were donated for further study, see Fig. 1. The sections were named Transition Joint and Fish # 11 and their location in the well and general specifications are presented in Table 1 and Fig. 2. Both sections were retrieved from the vertical part of the well where the slurry was bullheaded. It is generally assumed for vertical section that the pipe hangs vertically due to gravity and the eccentricity between the casings is not an issue (Guillot et al., 2008b). However, for both sections a significant eccentricity of the 9 5/8" casing relative to the 13 3/8" casing was found. After receiving the sections, a visual inspection was performed

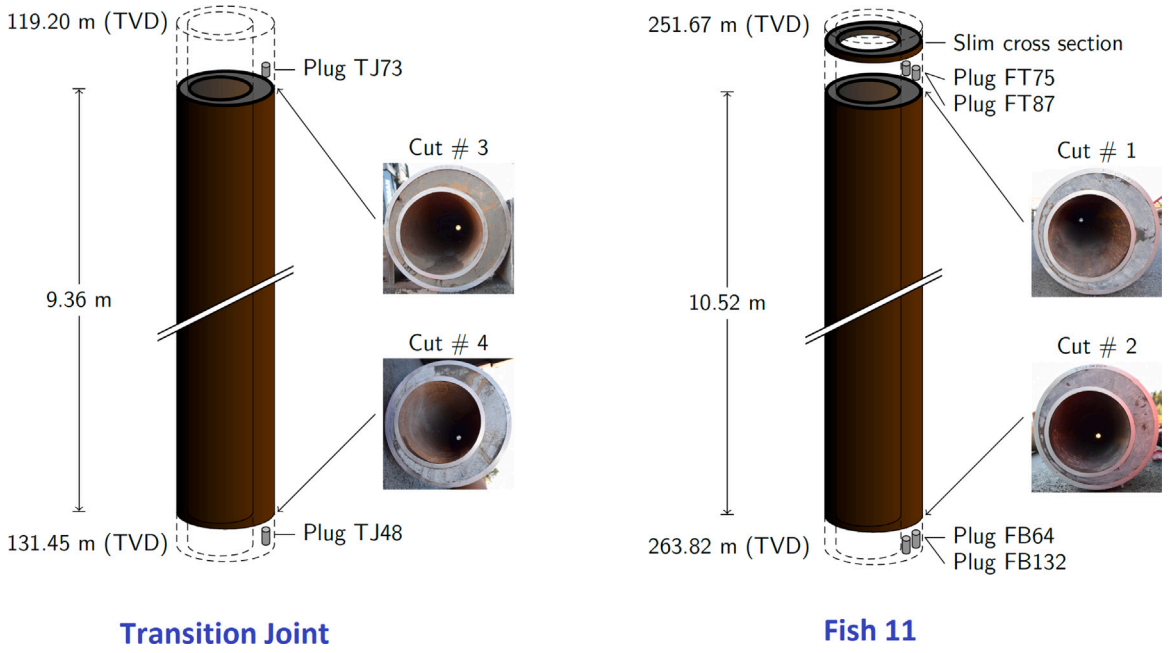

Fig. 2. Transition Joint and Fish # 11 diagram including pictures of the ends (Bottom and Top).

Table 1
Sandwich sections under study.

	Transition Joint	Fish # 11
Well depth (m)	119.2–131.5	251.7-263.8
Final length (m)	9.36	10.52
Min. Stand off (m)	0.01057	0.01250
Max. Eccentricity %	70	64

and the ends were dressed. The nomenclature of bottom and top was maintained according to the original recorded placement of the sections in the well, where the top is the shallowest well depth.

2.1. Transition joint

The shallowest section called the Transition Joint was recovered from 119.2 to 131.5 m well depth, see Fig. 2. The over pull applied during retrieval was 310 Klbs. This section contains the top of cement (TOC), the region where the interface between the original fluid in the well and the cement pumped into the annulus is found. The position of this interface can be challenging to localize,especially when washouts are present or substantial losses occur for the cementing job. Estimations based on the volume of cement slurry that was pumped into the well, predicted that the TOC should be found at 113 mTVD, whereas the results of surface re-logging using ISBL/VDL indicated that the true TOC was at 123 mTVD (Palacio et al., 2020). For the rest of the paper we assume the TOC as indicated by the logs.

Just above the TOC, the Cut # 3 was made, see Fig. 2. Here the annular space was filled with a brown colored material from mud solids, and empty spaces were observed on the narrow side of the annulus. At the bottom, the Cut # 4 was made; cement fully covering the annular space, and there was evidence of intrusions of brown material, see Fig. 2.

2.2. Fish # 11

The deepest section called Fish # 11, was recovered from the interval 251.7 to 263.8 m well depth, 140 m below the TOC, see Fig. 2. The over pull applied during retrieval was 500 Klbs. In this section a 9 5/8 casing collar was present 4.2 m above the bottom. Cut # 1 was made at the top and the Cut # 2 at the bottom. Cement covered the full annular space at the top and bottom. Local defects were present but were filled with mud solids; however the regions with mud intrusions looked less significant compared to the Transition Joint. At both ends there was evidence of cement debonding at the inner and outer casing surface, which appeared to be worst on the narrow side of the annulus.

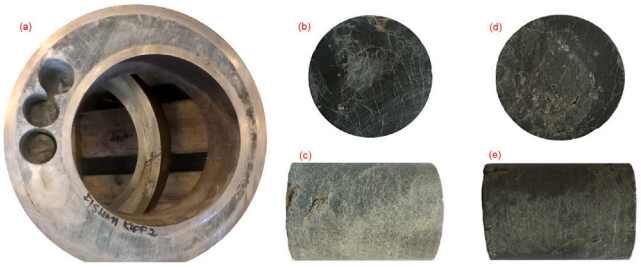

Fig. 3. Core plugs obtained from Fish 11 (Bottom). (a) Drilling of core plugs, (b) FB 64 top view, (c) FB 64 lateral view, (d) FB 132 top view and (e) FB 132 lateral view.

3. Material characterization and methods

The studied materials are divided in two parts. The first part corresponds to an in-depth characterization of core plugs drilled from the off-cuts removed when dressing the sandwich sections' ends. Cores were cut from the wider side of the sections, as is shown in Figs. 2 and 3. Table 2 presents an overview of the methods completed to characterize the core plugs, and the results allow a comprehension of the material bulk properties.

The second part includes the characterization of a slim sandwich cross-section cut from the top of Fish # 11, see Figs. 2 and 5, where it was possible to study the variations in cement properties around the annulus, not only on the wider side (as per core plugs) but also on the narrow side.

3.1. Core plugs

A total of 6 core plugs were drilled from the wider part of the annular space (as illustrated in Figure 3a) and recovered in satisfactory

Table 2
Overview of methods used to characterize the cement core plugs. CT: Computer Tomography Scanning, E:Young's Modulus, UCS: Uniaxial compressive strength, SEM: Scanning Electron Microscopy, EDS: Energy Dispersive Spectroscopy , XRF: X-ray Fluorescence, XRD:X-ray Diffraction.

Section name	Core plug	Petrophysical Properties			Mechanical Properties		Compositional Analysis		
		Porosity	Permeability	CT scan	E	UCS	SEM–EDS	XRF	XRD
Transition Joint	TJ48	✓	✓	✓	✓	✓	✓	✓	✓
	TJ73	✓	✓	✓			✓	✓	
Fish# 11	FT 75	✓	✓	✓	✓	✓	✓	✓	✓
	FT87	✓	✓	✓	✓	✓	✓	✓	✓
	FB64	✓	✓	✓				✓	
	FB132	✓	✓	✓					
Results can be consulted in:		Table 5	Tables 4, 3	Fig. 7 Table 6	Table 7	Table 7	Table 8 Figs. 9, 10	Table 9	Table 10

conditions. Four core plugs were recovered from the Fish # 11 section: two from the bottom (FB 64 and FB 132) and two from the top (FT 75 and FT87), as shown in the right panel in Fig. 2. From the Transition Joint, two additional core plugs were recovered (left panel in Fig. 2): one from the bottom (TJ 48) and the other one was taken from the material found above the TOC (TJ 73).

3.1.1. Petrophysical analysis

The core plugs were weighed in their initial condition (as drilled from the sandwich sections), cleaned with soxhlet extraction and subsequently dried at 60° C for several days until the weight was observed to stabilize indicating that pore fluids had been removed prior to gas permeability measurement. To measure the matrix volume, matrix density, pore volume and porosity, gas was allowed to enter the pore space of the cores from a container with a known volume at an initial pressure of 0.7 MPa. The calculations were made applying Boyle's law.

Gas permeabilities reported were measured by flooding the core plugs with nitrogen at a constant flow rate of 5 ml/min and measuring the obtained differential pressure drops across the cores. Most of the measurements were conducted at 2 MPa confining pressure. For each flow rate studied, permeability was defined using a stabilization criteria, which were reached when the differential pressure change across the cores was less than 10 Pa in a timeframe of 30 s. Stabilization time varies between 1 and 6 h.

The liquid permeabilities were estimated using the Klinkenberg correlation (Klinkenberg, 1941). This method is used for tight porous mediums where the permeability is in the range of millidarcy and gas permeability measurements are feasible and accurate (Moghadam and Chalaturnyk, 2014; Li and Sultan, 2017). Flow rates of 1, 5 and 10 ml/min were used. By plotting the gas permeability versus the reciprocal of the mean pressure it is possible to estimate the medium's liquid permeability (or permeability at infinite pore pressure) from the intercept using a linear fit,

$$K_g = K_l(1 + \frac{b}{P}), \quad (1)$$

where K_g is the gas permeability, K_l is the permeability of the medium at infinite pore pressure, P is the pore pressure and b is the gas slippage factor.

For the core FT 87 gas permeability was measured for different confining pressures 2, 5, 10 MPa to evaluate the effect of confining pressure. For one of the cores (FT 75) the liquid permeability was also measured directly by applying 2 MPa of confining pressure and pumping deionized water at 20 °Celsius (273.15 ° K).

3.1.2. Computed Tomography (CT) scanning

CT scans are widely used to characterize the distribution and connectivity of pores and fractures for reservoir rocks. However, more recently CT scans have been used to investigate the petrophysical properties of early age cement (Ueda et al., 2018; Bossa et al., 2015; Brisard et al., 2018; Yang et al., 2019). The apparatus Toshiba Aquilion Prime 80 was used to acquire images with a resolution of 500 μm for the 6 core plugs.

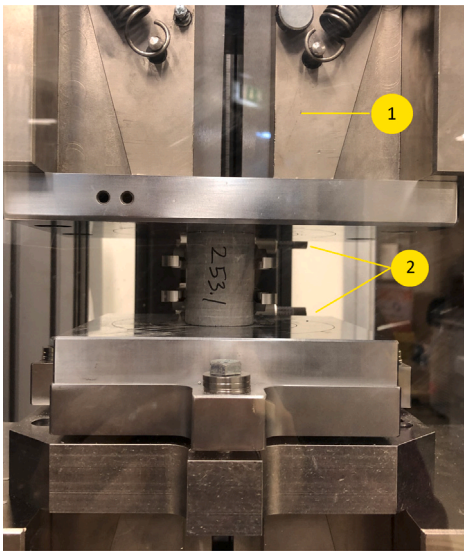

Fig. 4. Testing machine model *Instron 5985*. (1) core plug FT75 sample positioned for testing. (2) instrumentation with a deformation indicator type single column extensometer.

The core density determines the degree to which X-rays are attenuated, which directly affects the brightness and contrast of the images. Materials with high attenuation (strong absorption) are shown as white, while those with low attenuation (weak absorption) are black. The Hounsfield Unit Value (HUV) is used to quantify the attenuation. For rock samples, low HUV due to pore space and fractures is represented with a dark color whilst components with high density have high HUV and a light color.

3.1.3. Mechanical properties

After evaluation of petrophysical properties and CT Scans, three of the core plugs were exposed to uniaxial monotonic loading to determine the uniaxial compressive strength (UCS). The UCS and Young's modulus were determined for two core plugs from the top of the Fish # 11 section (FT 75, FT 87) and one from the bottom of the Transition Joint (TJ 48). The experiments were performed at the University of Stavanger (UIS), using an *Instron 5985* with force capacity of 250 kN. A constant displacement of 0.2 mm min^{-1} was set for the load cell and the core plugs were loaded until failure whilst recording the load with the Instron machine and the deformation using a Instron long travel extensometer for single column model Intron AUTOX 750 as illustrated in Fig. 4. Note that the dimensions of core plugs do not follow the ASTM D 2166-00 standard recommendation, where is suggested that the length should be 2 - 2.5 times the diameter of the core sample, but the strain rate used attends ASTM recommendation for standard core sizes.

Table 3
Measured gas permeability (Kg) for core plug FT 87 varying the confining pressure. Results are presented in milidarcies, for SI units use conversion factor (1 mD = $9.869\,23 \times 10^{-16}$ m^2).

Core plug	Permeability (mD)		
	at 2 MPa	at 5 MPa	at 10 MPa
FT 87	0.18	0.04	0.03

Table 4
Petrophysical properties: Permeabilities. Kg: Gas permeability, Kl: Liquid permeability-Klinkenberg, Kw: Measured Water permeability. Results are presented in millidarcy, for SI units use conversion factor (1 mD = $9.869\,23 \times 10^{-16}$ m^2)

Core plug	Porosity (%)	Kg (mD)	Kl (mD)	Kw (mD)
TJ 48	46.7	0.32	0.15	Not measured
TJ 73	1.6	≤ 0.001	≤ 0.001	Not measured
FT 75	38.4	0.29	0.21	0.02
FT 87	35.9	0.18	0.10	Not measured
FB 64	38.2	0.27	0.14	Not measured
FB 132	41.1	22.96	18.43	Not measured

3.1.4. Compositional analysis

After mechanical analysis, fragments of the samples were used to evaluate the cement chemical composition using different techniques: Scanning Electron Microscopy (SEM) and Energy Dispersive Spectroscopy (EDS), X-ray Fluorescence (XRF) and X-ray Diffraction (XRD).

Scanning Electron Microscopy (SEM) and Energy Dispersive Spectroscopy (EDS)

SEM–EDS analyses were used to examine the cement microstructure and composition. SEM was used to study morphology and EDS was used to perform a semi-quantitative analysis of the elemental composition. Fragments were analyzed using a Zeiss Supra 35VP field emission gun scanning electron microscope (FEG-SEM) fitted with an EDAX Octane Elite EDS system, located at UIS, Norway. The unpolished samples were coated with a thin layer of palladium to avoid charging of electrons during analyses and the equipment was set to an acceleration voltage of 15 kV, aperture size of 30 μm and working distance of 12 mm.

X-ray Fluorescence (XRF)

The fragments from one core from the Transition Joint (TJ 48) and two fragments from the top of Fish # 11 (FT 75 and FT 87) were used to obtain their elemental composition using X-ray Fluorescence. Measurements were made using a commercial benchtop spectrometer, the M4 Tornado located at the Universidade do Estado do Rio de Janeiro — UERJ, Brazil. This device has a Rhodium tube (air cooled), and an energy dispersive silicon drift detector with 30×10^{-5} mm^2 sensitive area. The system also has a polycapillary lens that provides a micro beam size of 25 μm. The equipment was operated at 35 kV and 600 μA with a 12.5 mm/Al filter. The acquisition time for each spectrum was 100 s and a vacuum of 2000 Pa was applied during the measurement. The model for the elemental quantification assumes a matrix of Calcium Carbonate ($CaCO_3$) and the analysis was performed in 5 aleatory points for each sample.

X-ray Diffraction (XRD)

The fragments from the core plugs were prepared in powder form and subsequently analyzed at the University of Stavanger, using a Bruker D8 Advance with a Lynxeye detector (Cu-K α radiation 1.5406 Kα1, 40 kV 25 μA, 0.6 mm receiving slit). The measurements were obtained in the range of 2 θ, from 8° to 90° in steps of 0.05° and 8 s per measurement.

The crystallographic analysis from the identified minerals was done in the data base PDF2 using the software X'pert Highscore and the crystalline phase content was quantified using the Rietveld refinement method in the software GSAS.

3.2. Slim sandwich cross-section

A 3 centimeter thick slim cross-section was cut from the top of Fish # 11, shown in Fig. 5. Eleven angular segments of approximately 33° were defined and numbered 1 through 11 on the sample to perform additional analysis (see nomenclature on Fig. 5). The characterization of this sample was performed in collaboration with the Museum of Archeology in Stavanger, Norway.

3.2.1. Compressive strength by rebound hammer

The rebound hammer method is based on the principle that the rebound of an elastic mass is a function of the hardness against the mass strikes. This non-destructive technique estimate the compressive strength of concretes based on the rebound index, which procedure is detailed in the ASTM C805 ("ASTM International, West Conshohocken, PA ", 2018). Other studies of applications of this technique for concrete mixtures have been reported by other authors (Szilágyi et al., 2014; Kumavat et al., 2021a). For this study, the measurements of rebound were made using a Schmidt hammer. The linear relation of rebound number with compressive strength was used to investigate the variations on cement strength around the cross-section. 30 measurements were obtained holding the hammer vertically. Three measurements were made in the center of the annular space for each segment, with the exception of segment 6 due to the reduced area. As an example, the yellow circles in Fig. 5 show the location of the measurements for segment 11.

3.2.2. Mapping using X-ray fluorescence (XRF)

A total of 80 measurements was made to characterize the composition using a Bruker Tracer III-SD handheld X-ray Fluorescence (XRF) spectrometer, as indicated by the red circles in Fig. 5. The instrument allows a non-destructive identification of elements from magnesium to uranium and semi-quantitative analysis. The measurements were carried out at 40 kV and 30 μA without using a vacuum system. Each measurement covers an area of 0.7 mm^2 and has a penetration depth of 0.7 mm below the surface. For the angular segments in the wider annulus region, numbered 1, 2, 3, 9, 10 and 11, nine measurements were taken (highlighted by red circles in Fig. 5. For the narrow annulus region segments, numbered 5, 6 and 7, three to five measurements were taken due to the reduced area.

Table 5
Petrophysical properties: Core plugs bulk properties.

Core Plug	Length (cm)	Diameter (cm)	Initial Weight (g)	Final Weight (g)	Pore Volume (mL)	Matrix Volume (mL)	Matrix Density (g mL^{-1})
TJ 48	5.08	3.75	99.49	76.58	26.15	29.81	2.57
TJ 73	4.60	3.75	159.77	Not measured	0.78	48.03	3.33
FT 75	4.92	3.75	105.76	89.04	20.93	33.53	2.66
FT 87	4.97	3.76	107.67	92.23	19.66	35.17	2.62
FB 64	5.14	3.75	103.75	92.01	21.66	35.01	2.63
FB 132	5.08	3.75	96.72	85.60	22.81	32.66	2.63

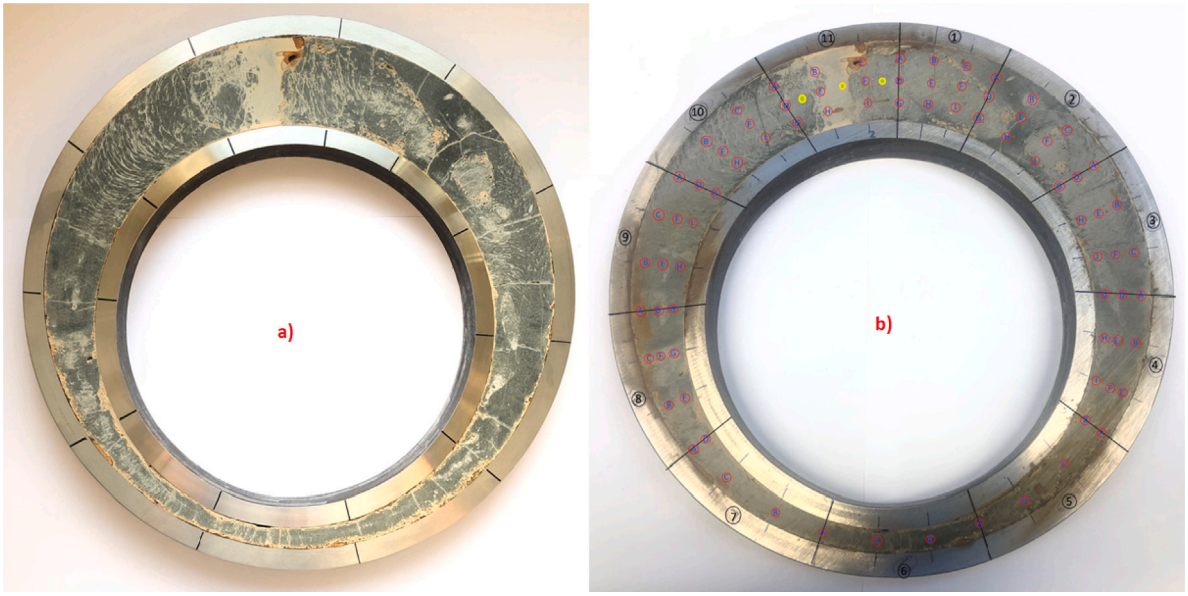

Fig. 5. Slim section recovered from the top of the Fish # 11 Section. a)High resolution picture b) section showing points of measurement for XRF in red and Rebound hammer in yellow. (For interpretation of the references to color in this figure legend, the reader is referred to the web version of this article.)

4. Experimental results

4.1. Core plugs

4.1.1. Petrophysical analysis

Core plug weights (initial and after drying), pore volume, matrix volume and density are presented in Table 5. Core plugs from the Fish # 11 section show small variations in pore and matrix volumes. The matrix density is also similar for all core plugs and cement density is estimated at $2.6\,g\,cm^{-3}$. For the Transition Joint the measured properties are significantly different compared to Fish # 11. The core TJ 73 has the highest matrix density of all the cores ($3.3\,g\,cm^{-3}$ and the core TJ 48 the lowest ($2.57\,g\,cm^{-3}$). These results appear to be consistent with the CT scan images for those core plugs, see Fig. 7. The plug TJ 73 is composed of higher density materials, while TJ 48 has a lower matrix density and a larger porous volume. Table 4 lists measured porosities plus gas (Kg and Klinkenberg (Kl)) and water (Kw) permeabilities. The porosity of the cement core samples varied from 46.7% in the bottom of the Transition Joint to between 35.9% and 41.1% for the core plugs retrieved from Fish # 11.

The gas permeability was measured at 2 MPa of confining pressure for all cores. For the Transition Joint core sample TJ 48, the gas permeability was estimated to be 0.32 mD ($3.15 \times 10^{-16}\,m^2$). Three of the four cores from Fish # 11 had gas permeabilities slightly lower than that from the Transition Joint, in the range 0.18-0.29 mD ($1.77 \times 10^{-16}\,m^2$ to $2.86 \times 10^{-16}\,m^2$). The core FB 132 has values of permeability two orders of magnitude higher than the other core plugs. Some authors suggest that mud contamination can increase the effective permeability of cement samples (Duguid et al., 2013; Katende et al., 2020). This observation agrees with the results of permeability and CT scans for the core plug FB 132, see Fig. 7, where core FB 132 exhibits higher contamination (with high and low density features from the CT scan) and the highest permeability of the core plug samples.

The additional analyses were done on the core FT 87 to measure the gas permeability at different confining pressures. The results suggest that the permeability decreased as pore pressure increased, see results in Table 3. This result highlights the importance of reporting the cement permeability along with the confining pressure applied.

Fig. 6 illustrates the estimation of liquid permeability (also known as Klinkenberg) for the core plug FB 132. Five gas measurements are used to obtain a linear regression, given by equation $K_g = 2.494(x) + 18.43$ with $R = 0.9965$, for which the intercept with the vertical axis corresponds to the liquid permeability.

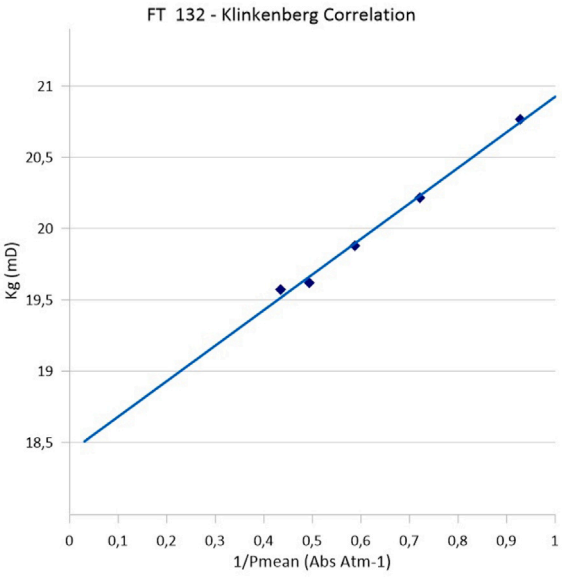

Fig. 6. Klinkenberg correlation for core plug FB 132. All measurement at 20 bar of confining pressure.

A similar procedure was performed for all cores. Estimated liquid permeabilities are between 0.1 mD and 0.21 mD ($9.87 \times 10^{-17}\,m^2$ to $2.07 \times 10^{-16}\,m^2$) for most of the cores. The results are presented in Table 4 and suggest that liquid permeability is always smaller than the measured gas permeability in steady state conditions. Time to reach steady state conditions, considering the stabilization criteria of 10 Pa in 30 s, varied between 1 to 3 h for the samples.

The Klinkenberg correlation for all the cores shows that the permeability to gas increases linearly with an increase of the inverse of pressure. This observation is consistent with the results obtained for tight reservoir rocks (Tanikawa and Shimamoto, 2006, 2009; Ren et al., 2016; Letham and Bustin, 2015; Shar et al., 2016). Klinkenberg permeability results for other samples of cement class G were not found

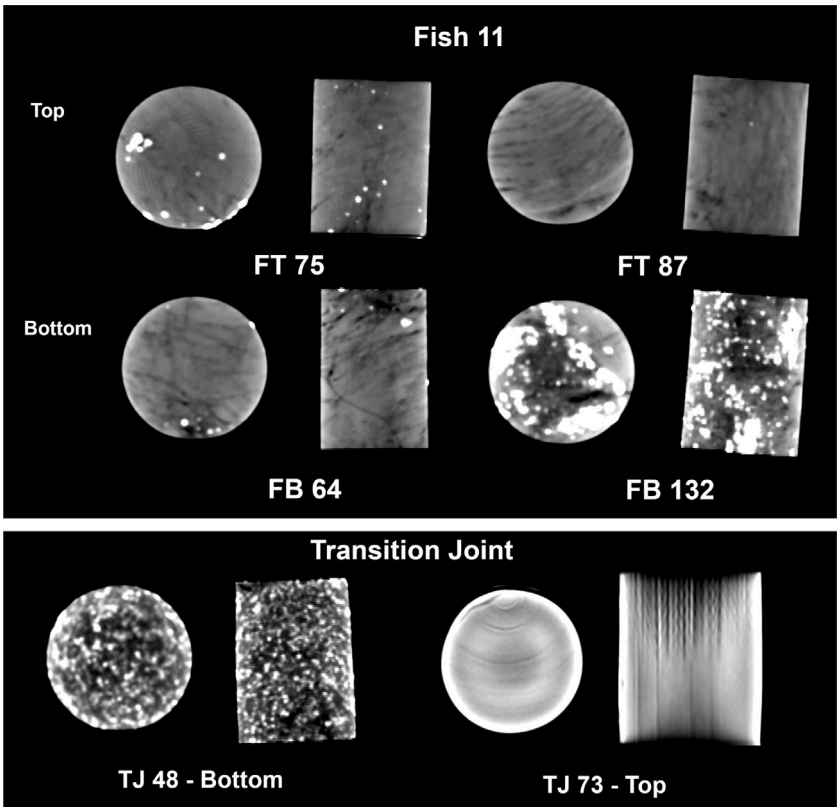

Fig. 7. CT scan for Fish # 11 and Transition Joint core plugs.

in the literature for comparison. Results for FT 75, FT 87, FB 64 and TJ 48 are consistent with results from gas, liquid and Klinkenberg liquid permeability obtained for sedimentary reservoir rocks. Where gas permeability is 2 to 10 times larger than water on the same specimen and gas permeability decreases with an increase in pore pressure (Tanikawa and Shimamoto, 2006, 2009). The results of water permeability for the core FT 75 show that permeability to nitrogen is 10 times larger than the permeability to water. The difference between the liquid permeability (estimated by the Klinkenberg correlation) and the measured water permeability may suggest the importance of interactions fluid–structure. Differences between both have been tried to be explained by heterogeneities in the porous media or phenomenons such as: slippage effects (Tanikawa and Shimamoto, 2009; Wang et al., 2014; Firouzi et al., 2014), wettability (Kumavat et al., 2021b), hysteresis and capillary forces (Ahrenholz et al., 2008). This observation highlights the need to extend the study of the Klinkenberg effects in very tight porous media such as cement, as has previously been studied in concrete materials by Zhou et al. (2015) and Loosveldt et al. (2002).

4.1.2. CT scan

CT scans for the 6 core plugs taken from both sections are presented in Fig. 7. The images shown are for the middle of the core plug in the radial and longitudinal directions. The maximum and minimum values of the Hounsfield scale for the plugs are presented in Table 6.

The core plugs from the top of Fish # 11 section (FT 75 and FT 87) show a similar response with few intrusions of high density material. Surprisingly, the CT scan for cores obtained from the bottom part of the section (FB 64 and FB 132) showed more heterogeneity and with significant differences between them especially considering that the core plugs were cut adjacent to each other. The core FB 64 showed sparse intrusions of material with high attenuation, and the material with low attenuation (pore space or low density material) was apparently interconnected and more present in the upper part of the plug. The core FB 132 showed a considerable content of high density material, partially agglomerated.

Table 6
CT Scan. Hounsfield Unit Value (HUV) for core plugs.

Core plug	Hounsfield Unit Value (HUV)	
	Min	Max
TJ 48	795	1766
TJ 73	3314	5446
FT 75	1207	1836
FT 87	112	1655
FB 64	941	1595
FB 132	518	1714

For the Transition Joint the core plug from the bottom part (TJ 48), also showed a significant content of both high and low density materials but it appears less aggregated than FB 132. The core plug TJ 73, above the TOC, is comprised of high density material.

HUV is a scheme for scaling the attenuation coefficients. Since there is no standardization, comparisons of results from different instruments and measuring conditions are difficult. However, based on the densities of the materials, predictions can be made. Some authors published typical values of Hounsfield scale for some mineral components (Cai, 2011). According to them, calcite, one of the main components of cement, typically shows 1861 HUV when the density is 2.71 g/mL. This number appears congruent with the upper limits of HUV obtained from the cores studied and the density reported in the previous section. The CT response for the core TJ 73 was associated with the presence of barite (also known as barium sulfate $BaSO_4$), that is a dense mineral used to increase the drilling mud density. The white spots in the cores FT 75, FB 64, FB 132 and TJ 48 represent intrusions of barite in the cement slurry, which was confirmed by the compositional analysis.

Table 7
Mechanical properties from core plug and reference values reported by Teodoriu and Asamba (2015).

Sample	Maximum UCS (MPa)	Young's Modulus (GPa)	Curing Time	In situ Conditions Temperature (C) - Pressure (MPa)
FT 75	26.9	6.74	33 years	10 - 3.7[a]
FT 87	42.8	7.45	33 years	10 - 3.7[a]
TJ 48	17.1	6.08	33 years	10 - 1.2[a]
Roy-Delage et al. (2000)	37	6.6	3 days	77-27
Morris et al. (2003)	40	4.4	3 days	84-27
Teodoriu et al. (2012)	60	17	60 days	75-0.1
Lesti et al. (2013)	45–60	17	6 months	90-40

[a]Values were assumed.

4.1.3. Mechanical properties

The results for UCS and Young's Modulus for core plugs FT 75, FT 87 and TJ 48 are presented in Table 7. The stress, strain response for Fish 11 samples is presented in Fig. 8. The results suggest that the cement in the Transition Joint has a lower resistance to compression, whilst the cement in Fish # 11 can support higher loading before failure. The curing conditions for FT 75, FT 87 and TJ 48 were estimated to be a pressure of 1.28 MPa for the Transition Joint (TVD of approx. 130 m, and a column of water above). For Fish # 11, considering a TVD of 260 m and assuming that the slurry below 130 m has 1.92 sg, the pressure on site was approximately 3.70 MPa. The curing temperature is more difficult to establish. However, the bottom sea temperature is around 4 °Celsius and the thermal gradient for the North Sea is estimated to be 4 °Celsius per 100 m (M.W.I.brahim, 1994; CORNELIUS, 1975). That, at the depths of the sections, indicates a temperature around 10–12 °C. So, for practical purposes a value of 10 degrees Celsius might be assumed for both sections. Nevertheless, the temperature after the well started production may be higher.

A comparison between the Valhall samples and results published by other authors, see Table 7, shows that the measured Young's modulus falls between the values reported for other samples with curing times between 3 days and 6 months. The compressive strength for FT 87 is also comparable with the references, suggesting a cement with good structural integrity.

The UCSs for the cores FT 75 and TJ 48 show a reduction of 32.75% and 42.75% compared to FT 87 and are lower than the reference values listed in Table 7 for Class G cement. This reduction in resistance may be associated with the mud contamination detected in the samples by the CT scan and the compositional analysis. This observation agrees with other studies that have found indications that UCS decrease with the increase of OBM content (Li et al., 2016; Eid et al., 2021). In a recent publication Katende et al. (2020) found that mud contamination of 10% and 30% reduced the UCS by 25% and 72%, respectively

The core plug FB 132 (from the bottom part of Fish # 11) was used for additional petrophysical studies and its mechanical properties have not yet been measured. The core FB 64 was fractured during transport and the core TJ 73 is unconsolidated, so that neither was suitable for mechanical properties analysis.

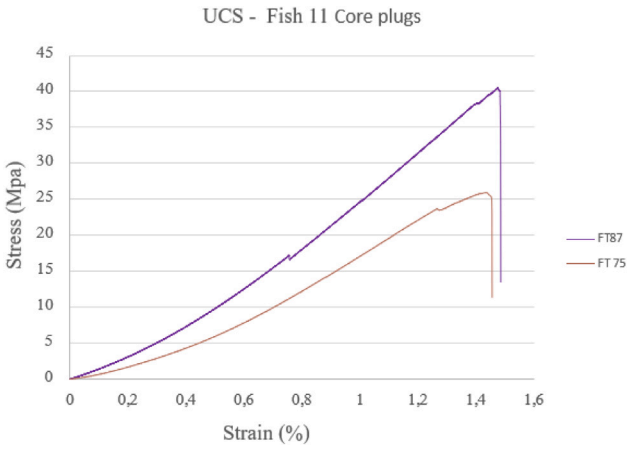

Fig. 8. Strain–Stress curve obtained when core plugs from the top of Fish 11 were submitted to monotonic compressive load (UCS test). Note that FT75 and FT87 where recover from cement at 253 m well depth and cut beside each other. Large Deviation is observed.

4.1.4. Microstructural and compositional analysis

SEM and EDS

Elemental compositions for 4 core plugs were obtained: For two core plugs from the top of Fish # 11 (FT 75, FT 87) and two cores from the Transition Joint (TJ48, TJ73). For each core two fragments were selected for high-resolution imaging at magnifications of 500 X, 1 kX and 10 kX. Fig. 9 shows the comparison of microstructure for samples with 1 kX magnification in the upper panels and 10 kX in the lower. Cement hydration products were identified as an homogeneous matrix with some angular morphologies that can be associated with the presence of calcium carbonate. In the images the bright matrix is typical for Portland cement hydration products (C-S-H and CH) with medium to light gray color.

EDS was used to identify the elemental distribution using spot and area modes. A total of 6 areas and between 65 and 70 spots per sample were analyzed. Typical elements in hydrated cement were found (Ca, Si, Al, S, C, O). Barium (Ba) is one of the elements composing barite ($BaSO_4$), an additive used in Oil Based Mud (OBM) and Water Based Mud (WBM) as a weighting material. The presence of this element can be used as a tracer to identify if the cement slurry was contaminated by mud or spacer fluid during the placement as this element is not typically present in Portland hydrated cement.

Table 8 shows the results of elemental concentration by atomic weight percent from the EDS area mode. Only the average values are reported. The results show that samples FT 87, FT 75 and TJ 48 have a similar elemental mean composition and are rich in calcium phases. There are high amounts of carbon, associated with calcium to form calcium carbonate ($CaCO_3$). The sample TJ 48, however, has a richer content of Ba, Cl, Na, Fe, S, K probably associated with mud contaminants and congruent with the CT scan. The sample TJ 73 shows a different elemental composition, rich in O, Ba and S and poor in calcium phases.

Fig. 10 shows the results of elemental concentration by weight percent using the EDS spot mode, for 140 spots from each section. The distribution of elements for the Transition Joint appears to be more dispersed, mainly for the contents of Ca, C, O, S and Ba. The Fish # 11 and Transition Joint show barium (Ba) content, implying some level of mud contamination in the slurry that is more represented in the Transition Joint. Higher content of sulfur (S) was also found in the Transition Joint, which is associated with the presence of barium sulfate (barite).

XRF

The results of elemental composition were converted to oxides and normalized to 100%, see Table 9. Results confirm the similarity in

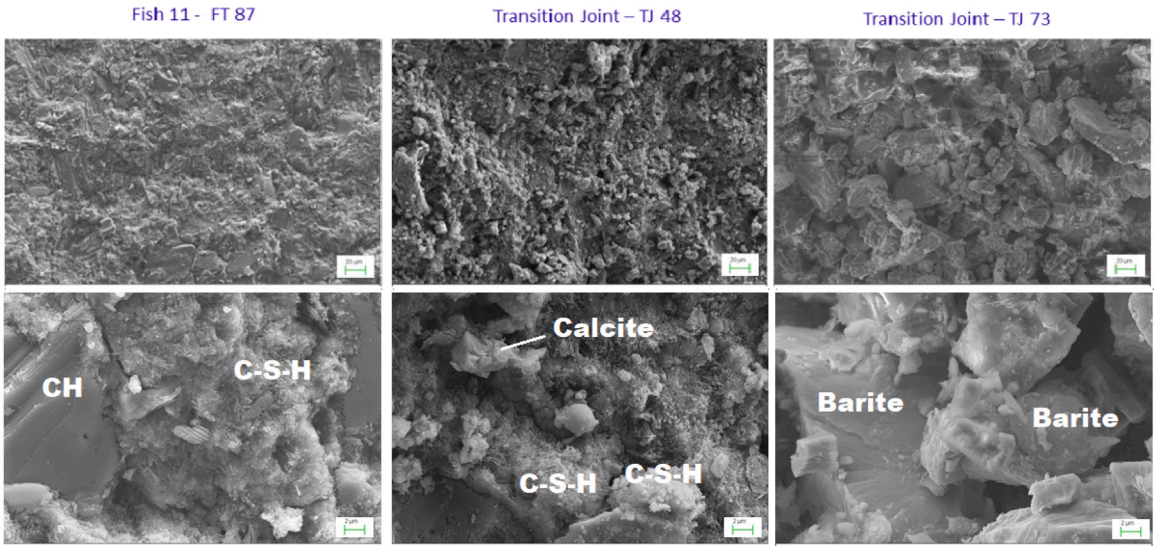

Fig. 9. Comparison of SEM Images at magnifications 1.0 kX (upper panels) and 10.0 kX (lower panels) for material extracted from FT87, TJ47 and TJ 73 core plugs.

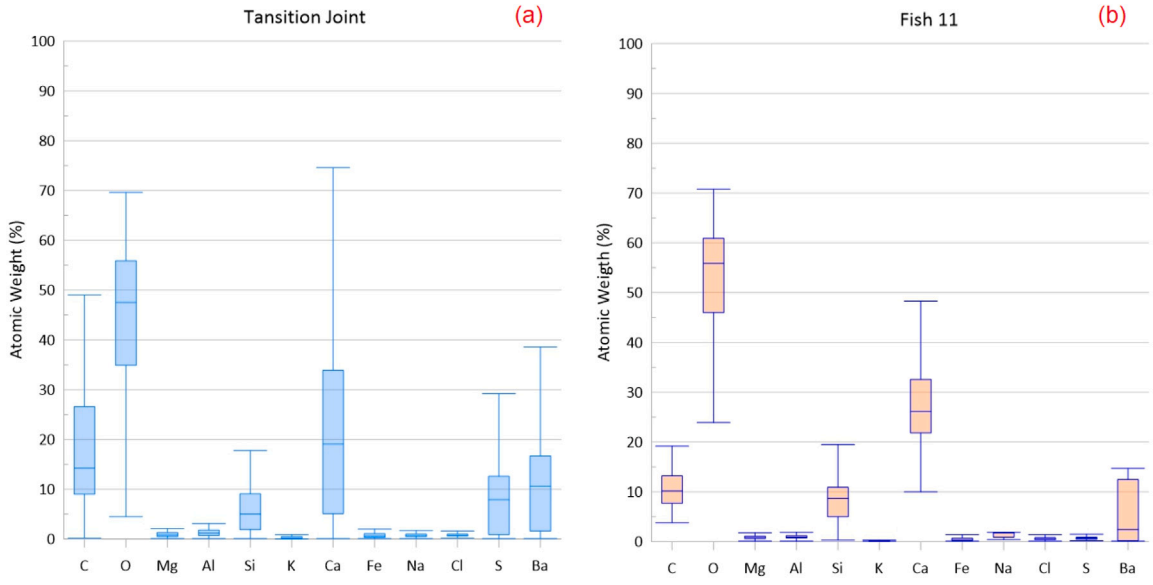

Fig. 10. Box plot of elementary atomic Weight for (a) Transition Joint and (b) Fish # 11. Results based on EDS for 140 spots.

Table 8
Semi-quantitative results of elementary concentration using SEM–EDS (content in weight percent).

Element	FT 75	FT 87	TJ 48	TJ 73
C	8.66	7.55	8.0	24.57
O	53.58	54.67	49.16	43.35
Mg	0.63	0.67	0.46	1.06
Al	0.93	1.12	1.28	1.45
Si	8.63	7.65	7.88	2.12
S	0.73	0.55	1.74	10.87
K		0.1	0.26	0.1
Ca	26.88	25.15	31.12	1.32
Fe	0.70	0.67	1.44	1.25
Na			0.1	
Cl	0.6	0.5	0.7	
Ba			1.34	13.87

composition of samples FT 75, FT 87 and TJ 48 and imply a high content of Ca, Si and Al, consistent with the presence of cement phases such as calcium silicate and calcium aluminates. The core plug TJ 73 appears to be mainly composed of barium components, supporting the findings from the CT scan and SEM/EDS.

Typical values from laboratory samples have been reported for Portland cement by Kosmatka and Panarese (1988), by Dueramae et al. (2019), and by Bahafid et al. (2017). From cement samples recovered from oilfield wells, Carey et al. presented the results of XRF for unaltered cement (which they named Gray cement 6545 and 6549) and degraded cement (named Orange cement 6549) (Carey et al., 2007). A comparison of the values is presented in Table 9, and it is seen that the Valhall samples present a lower content of silicon dioxide (SiO_2) and aluminum oxide (Al_2O_3) and levels below detection for magnesium oxide (MgO). The content of calcium oxide (CaO) is still close to 60 %, comparable both with the laboratory samples and the unaltered cement, which indicates that only minor degradation (decalcification) has occurred in the cement over time.

XRD

The X-ray diffraction patterns confirm the presence of both crystalline and amorphous phases. The amorphous fraction, evidenced by

Table 9
Quantitative results of oxides concentration in percentage normalized to 100%. LOI: Loss of Ignition (mass loss after cement sample is exposed to 1000 C°).

Oxide	Valhall samples				Laboratory samples (Bahafid et al., 2017)	Samples from SACROC Unit (Carey et al., 2007)[a]	
	FT 75	FT 87	TJ 48	TJ 73		Unaltered cement	Degraded cement
SiO_2	12.28	10.04	13.28	2.40	19.1	19.09	19.40
Al_2O_3	1.05	0.90	1.91	1.88	2.90	3.95	3.87
Fe_2O_3	3.44	3.77	3.87	0.92	3.70	2.15	2.04
CaO	62.63	64.92	59.93	0.50	67.2	53.65	43.80
NaO_2						1.91	3.19
SO_3	0.55	0.95	1.43		2.5		
TiO_2	0.25	0.29	0.28		0.4	0.20	0.19
K_2O	1.48	0.75	0.77	0.18			0.14
MnO	0.05	0.06	0.05			0.09	0.07
MgO					1.4	2.95	1.01
BaO				94.17			
Others	0.12	0.15	0.12		0.5	0.09	0.07
LOI	18.15	18.43	19.62	9.82	2.4	15.92	26.22

[a]Values were normalized including LOI.

Table 10
Crystalline phase quantification in percentage, obtained by XRD and Rietveld refinement.

Phase	FT 75	FT 87	FB 64	TJ 48
Barite	1.58	3.88	5.21	5.46
Belite	4.44	10.56	18.29	16.22
Calcite	24.70	22.39	35.67	15.00
Portlandite	51.95	31.07	34.46	28.90
Vaterite	17.33	32.10	6.37	31.03
Katoite	0.00	0.00	0.00	3.40
Total	100	100	100	100
$\chi 2$	17.37	24.57	26.34	23.26
wRp	0.031	0.0595	0.0594	0.0567

Table 11
Rebounded measurements and equivalent compressive strength.

Angular segment	Average rebound	Compressive strength (MPa)
1	40	45
2	52	56
3	54	64
4	47	56
5	38	43
6	Not measured	Not measured
7	40	44
8	47	57
9	49	58
10	45	51
11	39	40

a hump between 20 and 35 degrees (2 θ), corresponds to the short range structures from the Calcium Silicate Hydrate (C-S-H), formed as the main hydration product of Portland cement. The crystalline fraction was found to be composed of belite (Ca_2SiO_4) from residual anhydrous clinker, portlandite ($Ca(OH)_2$) which is a byproduct from the C-S-H precipitation, katoite ($Ca_3Al_2(SiO_4)1.5(OH)_6$) from the hydration of calcium aluminates, and calcite and vaterite, two polymorphs of calcium carbonate ($CaCO_3$) from the carbonation process of portlandite. Barite was also identified, which confirms the intrusion of mud in the cement slurry. XRD patterns with identification of phases are presented in Fig. 11. XRD analysis for TJ 73 showed mostly content of barite, and the results for this sample are not included in Table 10. Small amounts of barium bromide hydrate ($BaBr_2H_2O$) and Friedel's salt ($Ca_2Al(OH)_6Cl(H_2O)2$) were also identified in all samples; these can be associated with the presence of chlorine and bromine in sea water in the trapped brine. The FB 64 sample also contained some ettringite ($Ca_6Al_2(SO_4)_3(OH)_{12}\,26H_2O$), which can be associated with the calcium aluminates from clinker. Due to the small amount of these three salts in the samples, they could not be quantified by the Rietveld refinements.

Regarding the phase quantification, results show a predominance of calcium carbonate, comprising between 42 and 55% of the crystalline phases in the studied samples. These, together with the content of portlandite, indicate the development of a slow rate of carbonation over the years, and possibly a low temperature phase transition from vaterite to calcite, since the first is a metastable phase of the latter. Finally, the observed contents of belite are consistent with an advanced hydration process, where all the more reactive phases of alite, C3 A and C4AF have fully reacted, while the slow rate hydration of belite is still occurring. The phase quantitification per sample is presented in Table 10.

4.2. Slim sandwich cross-section

4.2.1. Compressive strength measurements by rebound hammer

A total of 30 rebound measurements were made holding the Schmidt hammer vertically. Results of the average rebound for each angular segment and the equivalent compressive strength range from 40 to 64 MPa. More details can be found in Table 11 and Fig. 13. The results agree within an order of magnitude with UCS obtained for the core plug FT 87, see Table 7, but also with the values reported by Teodoriu and Asamba (2015), Teodoriu et al. (2012). In their results, the maximum uniaxial compressive strength for pure cement class G mixed with fresh water reached 60 MPa while cement mixed with salty water gave a reduction to 30 MPa. Sea water was used to prepare this slurry and the cement contained intrusions of mud that reduced the mechanical strength.

The results of equivalent compressive strength obtained with rebound hammer measurements can be useful to obtain the initial estimations of mechanical properties. However, they may overlook the loss of strength due to local mud contamination that was observed in the UCS for the core plugs tested and discussed in Section 4.1.3.

4.2.2. Elemental mapping using XRF

The elemental composition and their azimuthal and radial variations where measured and discussed. Elements such as Al, Ba, Br, Ca, Cl, Fe, K, Mn, S , Si and Sr were detected in the sample. A vector analysis was performed using the results of the relative weight percentages of each element. Fig. 12 shows the distribution of typical elements present in cement. Calcium was the most abundant element detected with relative percentages between 64 and 78%. Aluminum and silicon represented less relative percentages with 0.4–0.5% and 0.84–0.90%, respectively. The results suggest that the distribution in the azimuthal and radial direction of those elements was mostly homogeneous. This agrees with the abundance of calcium phases found in the core plug results.

A similar analysis for other elements is presented in Fig. 13. The distribution of elements such as bromine, chlorine, barium and potassium is presented. The results suggest that the distribution of these elements is more heterogeneous along the radial and azimuthal directions.

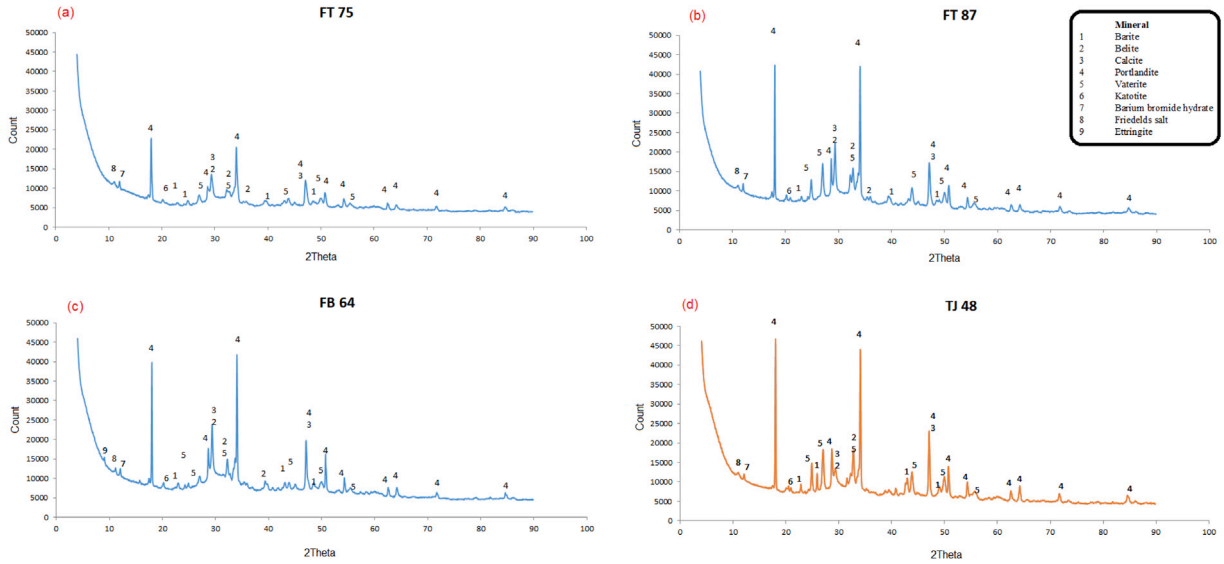

Fig. 11. X-ray Diffraction pattern phase identification comparison (a) FT75, (b) FT87, (c) FB64, (d) TJ 48. (For interpretation of the references to color in this figure legend, the reader is referred to the web version of this article.)

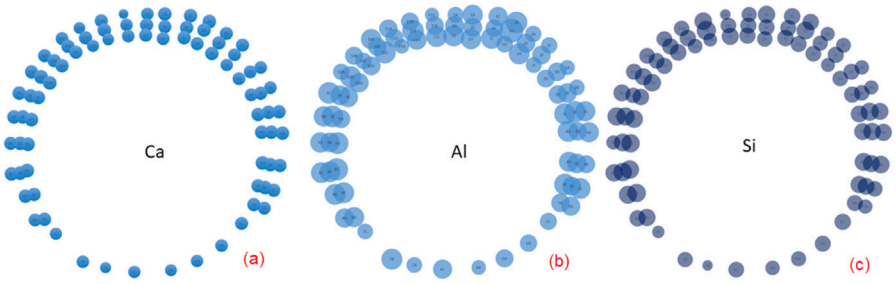

Fig. 12. Distribution of (a) Ca, (b) Al and (c) Si on the surface of the slim sandwich cross section.

Chlorine and bromine are elements typically present in sea water and their presence in the sample is consistent with the fact that the slurry was originally prepared with sea water. However, the different patterns in the distribution of those elements might suggest the location of migration paths where the $CaBr_2$ brine was trapped between the 9 5/8-in and 13 3/8-in casings. The distribution of potassium is more complex to explain as this element is added to cement slurries and drilling muds through additives such as potassium chloride. However, it appears to be less abundant in angular segments 4, 8 and 9.

An important variation in the barium content was found for the adjacent angular segments 1 and 11. The richer content of barium in segment 11 and poorer content in segment number 1 can explain why the cores FB 64 and FB 132 have a very different response in the CT scan, see Fig. 7. This is also in agreement with the different barium levels detected by SEM, XRF and XRD analysis for both core plugs. The slim sandwich cross-section was cut just a few centimeters above where the core plugs were drilled in the top of Fish # 11.

Fig. 13, bottom right, shows the results of compressive strength measured with the rebound hammer and indicated in red and green numbers around the cross section. The segments with lower resistance (1, 11, 5 and 7) correlates well with variations in levels of Br, Cl, K, and Ba. On the other hand, segments 3 and 9 show lower amounts of these elements. This observation suggests that contamination of the slurry may have an influence on the compressive strength.

5. Durability discussion

Important indicators of well barrier failure due to cement degradation are: appearance of fluid migration paths, loss of cement mechanical strength, increases in permeability and porosity and aggressive changes in cement phases (such as reduction of portlandite and decalcification) (Kiran et al., 2017; Shenold and Teodoriu, 2016). The appearance of those phenomena is normally difficult to track due to their interdependency and intercorrelation, as well as their variability as a function of the initial pore structure and curing conditions. Ferreira et al. (2019) presented a complete study of cement durability in the long term perspective for cement barriers. A modified version of their conceptual map is presented in Fig. 14, focused on long term durability for oil and gas cement well barriers. The results presented in the previous section are discussed in light of this conceptual map with the aim of understanding signs of degradation or alteration and possible causes.

The loss of cohesion and mechanical resistance are important symptoms of cement degradation that can lead to barrier failure, as shown by item B in Fig. 14. Other studies have suggested a decrease in compressive strength over time at high temperatures (Noik and Rivereau, 1999). In the present study, at relatively low curing temperature, mechanical properties such as maximum UCS and Young's modulus were comparable to early age cement (see Section 4.1.3), and the reduction in mechanical strength was shown to be affected mainly by localized slurry contamination. Consequently, the mechanical properties for the tested core plugs suggest only a low degree of degradation or alteration affecting structural integrity. This looks to be in agreement with findings of other authors were cement exposed to brine showed no critical alteration on cement (Vrålstad et al., 2016)

High values of permeability and porosity are expected when cement has been damaged or has integrity problems, as per item C in Fig. 14. Such alteration occurs especially when water penetration or aggressive ions (such as sulfate, chloride, magnesium, and others)

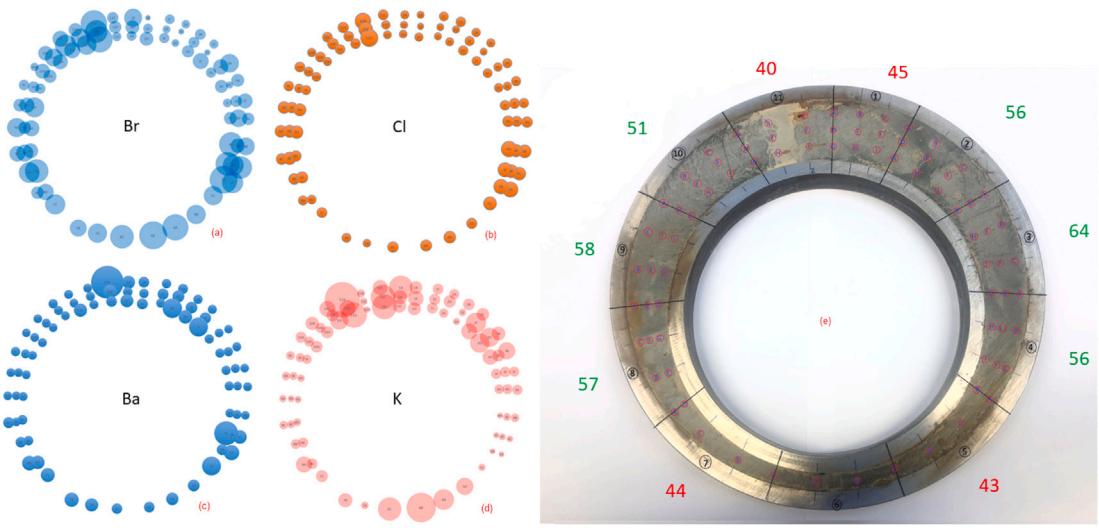

Fig. 13. Distribution of elementary composition for (a) bromine, (b) chlorine, (c) barium and (d) potassium and (e) Average compressive strength (MPa).

intrude the porous structure, reacting with cement and leading to deleterious chemical reactions weakening the material. The results of petrophysical properties presented in this work, Section 4.1.1, do not indicate significant cement alteration or degradation. The porosity and majority of the gas permeability measurements agree well with comparable values from other cement samples recovered from fields, such as those reported by Carey et al. (2007) and Duguid et al. (2013), and the bulk permeability for early age cement recently reported by Yang et al. (2019). The field cement samples analyzed and reported as "degraded cement" by Duguid et al. (2013) have porosity reaching 63% and permeability above 4.63 mD. Such values are almost twice the magnitude reported for the Valhall samples in the current work.

Changes in the contents of cement phases, such as decrease in calcium (decalcification), decrease in portlandite (leaching) and increase in calcite (that forms as a product of the consumption of portlandite) are also strong evidence of initial material degradation. As the initial content of the cement phases in situ is unknown, the direct comparison of initial conditions versus current condition is difficult. However, as presented in items 18 and 19 in Fig. 14, those changes can be an early sign of alteration or degradation. This can later on lead to material weakening and increase of permeability. The results of chemical characterization (SEM, EDS, XRF and XRD), Sections 4.1.4 and 4.2.2 , suggest that the slow rate of carbonation that had occurred over the 33 years had not significantly affected the cement integrity. The observations indicate that the levels of portlandite and calcite (from XRD) and content of CaO (from XRF) are comparable with laboratory and field samples reported by other authors, such as Carey et al. (2007), Lécolier et al. (2007), Duguid et al. (2013) and Scherer et al. (2011).

No corrosion or chemical attacks were observed on the cement porous matrix in the interfaces between cement or casings when the fresh cuts were made. This may suggest that the risk of in situ ion attacks leading to corrosion is low.

6. Conclusions

The results presented in the previous sections illustrate the difficulty of understanding the degradation and durability of cement samples, in particular under downhole conditions. However, this work can provide a baseline for future comparisons of results to assess old age cement from oil and gas wells.

The Elemental compositional analysis conducted by SEM, EDS, XRD and XRF has proved to be a powerful tool to understand the degree of contamination and degradation in the samples. Mechanical property measurements in combination with elemental analysis were able to explain the variations in the compressive strength.

The analyses performed on core plugs were limited to the material contained in the wider part of the annular space. The evaluation of the slim cross-section provided a better understanding of the azimuthal and radial variations in the cement properties and composition.

Despire the large dispersion in the mechanical properties of the samples, the cement recovered and studied in this work was shown to have the mechanical and chemical structural integrity required to prevent fluid flux through the bulk cement matrix after 33 years of downhole exposure. Nevertheless, the record of SCP in the well prior to abandonment is an indication that factors such as the existence of preferential fluid migration paths, can affect the well barrier integrity even when the bulk cement properties appears to have low degradation. The performed analyses showed that the overall decrease in cement matrix integrity was low, suggesting that the main migration paths, responsible for zonal isolation loss and seepage, might occur in the cement–casing interface, as discussed by Skadsem et al. (2020, 2021). Those results are in agreement with previous research from Bourgoyne et al. (2008) and Jung et al. (2013).

7. Future work

The authors strongly recommend that more cement samples that have been exposed to downhole conditions, should be recovered for study using the techniques presented in this paper. This will contribute to a better understanding of the aging effects and degradation of cement in well environments, specially in cases where detailed documentation of well integrity issues exist. The differences found between water permeability and gas permeability on cement, suggest that interactions between pore structure and fluids may be relevant for further studies. Still, a questions for future research is the durability of the wellbore cement over hundreds and thousands of years after well abandonment.

Acknowledgments

The Research Council of Norway, the Petroleum Safety Authority Norway, AkerBP, Conoco Phillips, Petrobras, Shell and Total are acknowledged for financing the work through PETROMAKS2, Norway project number 308767/E30 and the P&A Innovation Program, Norway – a program for accelerating P&A technology development. AkerBP is thanked and acknowledged in particular for providing the Transition Joint and Fish # 11 sections for the current and future studies.

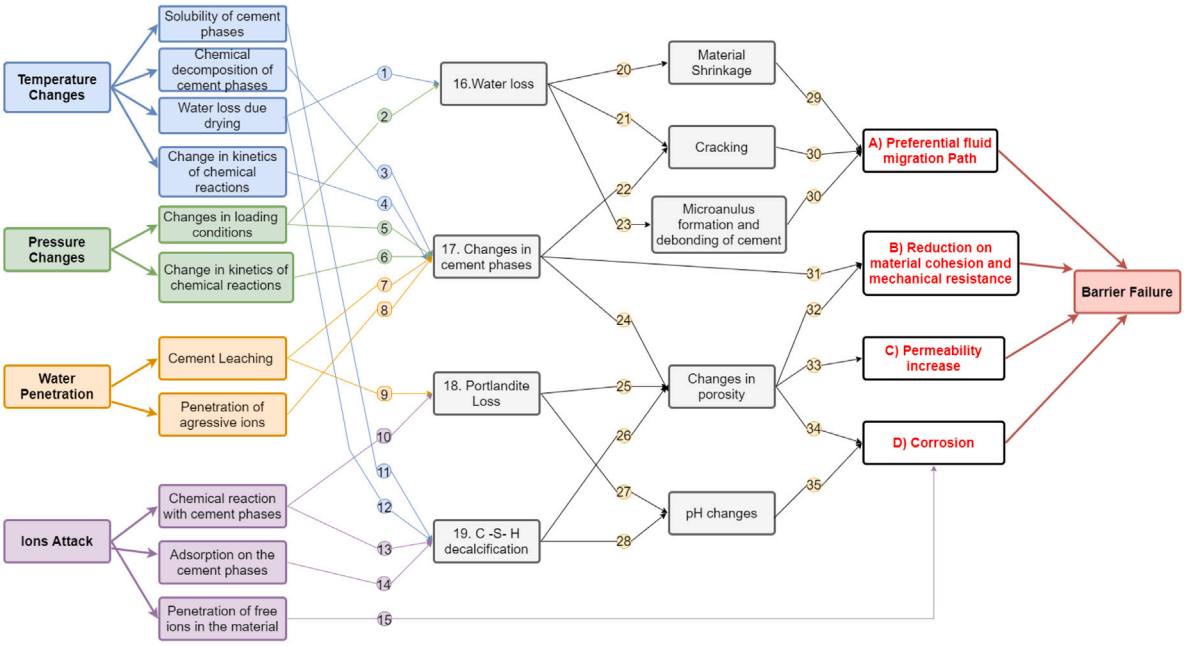

Nomenclature				
1. Loss of Water due to drying at high temperatures	8. Penetration of ions and reactions with cement hydration compounds.	15.Chloride and carbonate penetration increases the corrosion of metallic structures.	22. Changes in cement phases leading to volumetric changes and cracking.	29. Shrinkage of cement causes detachment of the material and leads to the formation of a preferential pathway between cement and geological setting or steel casing.
1. Loss of Water due to drying at high temperatures	8. Penetration of ions and reactions with cement hydration compounds.	15.Chloride and carbonate penetration increases the corrosion of metallic structures.	22. Changes in cement phases leading to volumetric changes and cracking.	29. Shrinkage of cement causes detachment of the material and leads to the formation of a preferential pathway between cement and geological setting or steel casing.
2. Loss of water due to reduction in the pore space	9. Loss of calcium from Portlandite. Reduces pH of the pore water.	16. Loss of water. Lead to shrinkage and cracking	23. Loss of water contract the cement, allowing the creation of debonding between casing and cement	30. Cracking and Microannuli leads to the formation preferential pathway
3. Chemichal decomposition at temperatures above 100 Celsius	10.Reactions that consume Portlandite. Sulfate, chloride and magnesium attack.	17. Changes in the cement phases. Loss of resistance and cohesion, cracking, porosity and permeability changes	24. Changes in cement phases leading to volumetric changes and cracking.	31. Changes at cement phases lead to loss of resistance and cohesion by the formation of non-cementitious phases (as M-S-H).
4. Lower Hydratation degree in the long term. favors deleterious reaction, as delayed ettingite Formation (DEF)	11. Solubility changes of crystalline phases. Loss of calcium.	18. Loss of Portlandite. Reduces pH and changes porosity and pore forms.	25. Loss of calcium from Portlandite and changes in the porosity due to the formation of expansive products.	32.Widening of pore size distribution and porosity lead to loss of resistance and cohesion.
5. Microstructural changes by C–S–H can cause dvolumetric changes on the cement as contraction and deformation.	12. Shrinkage due to water loss at C–S–H layers. Changes in the Ca/Si ratio.	19. C–S–H decalcification. Produce changes on pH and porosity and pore forms.	26. C–S–H decalcification leading to changes in the porosity due to the formation of expansive products.	33. Increases in porosity, normally leads to increases in permeability
6. Lower hydration degree in the long term. Favors carbonation reactions	13.Reduction of calcium in pore water. Changes in the Ca/Si ratio of C–S–H.	20. Shrinkage due to loss of water	27. Change of pH of pore water by loss of calcium and hydroxide ions.	34.Widening of pore size distribution and porosity lead to a higher penetrationof aggressive ions, increasing corrosion of metallic structures
7.Leaching and calcium loss. Formation of phases as brucite and M-S-H.	14. Calcium substitution in C–S–H. Decalcification.	21. Loss of water leads to cracking	28. Change of pH of pore water by loss of calcium and hydroxide ions.	35. Reduction of pH in pore water reduces the passivation layer provided by cement what increases the corrosion of metallic structures.

Fig. 14. Conceptual map of cement long term durability leading to well barrier failures. The fluxogram presented was modified using as a based the study developed by Ferreira et al. (2019).

We acknowledge the Electron Microscopy Nucleus of COPPE at Federal University of Rio de Janeiro (UFRJ), the Instituto de Fisica Armando Dias Tavares at the Universidade do Estado do Rio de Janeiro (UERJ), in Brazil and the Electron microscopy Laboratory at the University of Stavanger (UiS) in Norway for their support with the use of their microscopes and equipment. Professor Marcelino José dos Anjos at UERJ, Engineers Jørgen Grønsund and Dagfinn Sleveland at University of Stavanger, and Ali Mehrabi and Mohamed Mousa at NORCE are especially thanked for their collaboration during the experimental work.

We would also like to acknowledge the Coordenação de Aperfeiçoamento de Pessoal de Nivel Superior (CAPES) – Brazil. Part of this work was conducted during a scholarship supported by the Program CAPES/PDSE 47, Process 88881.187006/ 2018-01.

References

Agbasimalo, N., Radonjic, M., 2012. Experimental study of portland cement/rock interface in relation to wellbore stability for carbon capture and storage CCS. In: 46th U.S. Rock Mechanics/Geomechanics Symposium, 24-27 June, Chicago, Illinois.

Ahrenholz, B., Tölke, J., Lehmann, P., Peters, A., Kaestner, A., Krafczyk, M., Durner, W., 2008. Prediction of capillary hysteresis in a porous material using lattice-Boltzmann methods and comparison to experimental data and a morphological pore network model. Adv. Water Resour. 31 (9), 1151–1173. http://dx.doi.org/10.1016/j.advwatres.2008.03.009, Quantitative links between porous media structures and flow behavior across scales, URL https://www.sciencedirect.com/science/article/pii/S0309170808000511.

AkerBP, 2018. Annual Report 2018. Tech. rep., Aker BP SA.

Andrade, J.D., Sangesland, S., Skorpa, R., Todorovic, J., Vrålstad, T., 2016. Experimental laboratory setup for visualization and quantification of cement-sheath integrity. SPE Drill. Complet. 31 (04), 317–326. http://dx.doi.org/10.2118/173871-pa.

"ASTM International, West Conshohocken, PA ", 2018. ASTM 805/C805M-18: Standard test method for rebound number of hardened concrete. http://dx.doi.org/10.1520/C0805_C0805M-18, URL https://www.astm.org/Standards/C805.

Bahafid, S., Ghabezloo, S., Duc, M., Faure, P., Sulem, J., 2017. Effect of the hydration temperature on the microstructure of class G cement: C-S-H composition and density. Cem. Concr. Res. 95, 270–281. http://dx.doi.org/10.1016/j.cemconres.2017.02.008.

Barkved, O., Heavey, P., Kjelstadli, R., Kleppan, T., Kristiansen, T.G., 2003. Valhall field - still on plateau after 20 years of production. In: Offshore Europe. Society of Petroleum Engineers, http://dx.doi.org/10.2118/83957-ms.

Bossa, N., Chaurand, P., Vicente, J., Borschneck, D., Levard, C., Aguerre-Chariol, O., Rose, J., 2015. Micro- and nano-X-ray computed-tomography: A step forward in the characterization of the pore network of a leached cement paste. Cem. Concr. Res. 67, 138–147. http://dx.doi.org/10.1016/j.cemconres.2014.08.007.

Bourgoyne, A.T., Scott, S.L., Manowski, W., 2008. A review of sustained casing pressure occurring on the OCS. http://dx.doi.org/10.1021/es3012707.

Bourgoyne, A., Scott, S., Regg, J., 1999. Sustained casing pressure in offshore producing wells. In: Offshore Technology Conference. Offshore Technology Conference, http://dx.doi.org/10.4043/11029-ms.

Brisard, S., Davy, C.A., Michot, L., Troadec, D., Levitz, P., 2018. Mesoscale pore structure of a high-performance concrete by coupling focused ion beam/scanning electron microscopy and small angle X-ray scattering. J. Am. Ceram. Soc. http://dx.doi.org/10.1111/jace.16059.

Buzzi, O., Boulon, M., Hervé, M., Su, K., 2007. Leaching of rock-concrete interfaces. Rock Mech. Rock Eng. 41 (3), 445–466. http://dx.doi.org/10.1007/s00603-007-0156-5.

Cai, M., 2011. In: Taylor and Francis Group (Ed.), Rock Mechanics: Achievements and Ambitions. Taylor & Francis Ltd., Page 246, URL https://www.ebook.de/de/product/24342834/rock_mechanics_achievements_and_ambitions.html.

Carey, J.W., Wigand, M., Chipera, S.J., WoldeGabriel, G., Pawar, R., Lichtner, P.C., Wehner, S.C., Raines, M.A., Guthrie, G.D., 2007. Analysis and performance of oil well cement with 30 years of CO2 exposure from the SACROC unit, west texas, USA. Int. J. Greenhouse Gas Control 1 (1), 75–85. http://dx.doi.org/10.1016/s1750-5836(06)00004-1.

Chen, Z., Chaudhary, S., Shine, J., 2014. Intermixing of cementing fluids: Understanding mud displacement and cement placement. In: IADC/SPE Drilling Conference and Exhibition. Society of Petroleum Engineers, http://dx.doi.org/10.2118/167922-ms.

CORNELIUS, C.-D., 1975. Geothermal aspects of hydrocarbon exploration in the North Sea Area. URL https://openarchive.ngu.no/ngu-xmlui/bitstream/handle/11250/2674998/NGUnr_316_Bulletin_29_Cornelius_29_67.pdf?sequence=1&isAllowed=y.

Crow, W., Carey, J.W., Gasda, S., Williams, D.B., Celia, M., 2010. Wellbore integrity analysis of a natural CO2 producer. Int. J. Greenhouse Gas Control 4 (2), 186–197. http://dx.doi.org/10.1016/j.ijggc.2009.10.010.

Dueramae, S., Tangchirapat, W., Sukontasukkul, P., Chindaprasirt, P., Jaturapitakkul, C., 2019. Investigation of compressive strength and microstructures of activated cement free binder from fly ash - calcium carbide residue mixture. J. Mater. Res. Technol. 8 (5), 4757–4765. http://dx.doi.org/10.1016/j.jmrt.2019.08.022.

Duguid, A., 2009. An estimate of the time to degrade the cement sheath in a well exposed to carbonated brine. Energy Procedia 1 (1), 3181–3188. http://dx.doi.org/10.1016/j.egypro.2009.02.101.

Duguid, A., Butsch, R., Carey, J.W., Celia, M., Chugunov, N., Gasda, S., Ramakrishnan, T., Stamp, V., Wang, J., 2013. Pre–injection baseline data collection to establish existing wellbore leakage properties. Energy Procedia 37, 5661–5672. http://dx.doi.org/10.1016/j.egypro.2013.06.488.

Duguid, A., Radonjic, M., Bruant, R., Mandecki, T., Scherer, G., Celia, M., 2005. The effect of CO2 sequestration on oll well cements. In: Greenhouse Gas Control Technologies 7. Elsevier, pp. 1997–2001. http://dx.doi.org/10.1016/b978-008044704-9/50258-5.

Duguid, A., Scherer, G.W., 2010. Degradation of oilwell cement due to exposure to carbonated brine. Int. J. Greenhouse Gas Control 4 (3), 546–560. http://dx.doi.org/10.1016/j.ijggc.2009.11.001.

Eid, E., Tranggono, H., Khalifeh, M., Salehi, S., Saasen, A., 2021. Impact of drilling fluid contamination on performance of rock-based geopolymers. SPE J. http://dx.doi.org/10.2118/205477-PA.

Ferreira, E.G., Marumo, J.T., Franco, M.K., Yokaichiya, F., Vicente, R., 2019. 10000 years cement – can hydrated cement last as much as long-lived radionuclides? Cem. Concr. Compos. 103, 339–352. http://dx.doi.org/10.1016/j.cemconcomp.2019.05.016.

Firouzi, M., Alnoaimi, K., Kovscek, A., Wilcox, J., 2014. Klinkenberg effect on predicting and measuring helium permeability in gas shales. Int. J. Coal Geol. 123, 62–68. http://dx.doi.org/10.1016/j.coal.2013.09.006, Special issue: Adsorption and fluid transport phenomena in gas shales and their effects on production and storage, URL https://www.sciencedirect.com/science/article/pii/S0166516213002115.

Garnier, A., Laudet, J.B., Patil, S., Patil, R., Ravi, K., Ferreira, L., 2012. Effect of acid gas on cement sheath integrity: Experimental findings. In: SPE Saudi Arabia Section Technical Symposium and Exhibition. Society of Petroleum Engineers, http://dx.doi.org/10.2118/160890-ms.

Guillot, D.J., Froelich, B.G., Caceres, E., Verbakel, R., 2008a. Are current casing centralization calculations really conservative?. In: IADC/SPE Drilling Conference. Society of Petroleum Engineers, http://dx.doi.org/10.2118/112725-ms.

Guillot, D.J., Froelich, B.G., Caceres, E., Verbakel, R., 2008b. Are current casing centralization calculations really conservative?. In: IADC/SPE Drilling Conference. Society of Petroleum Engineers, http://dx.doi.org/10.2118/112725-ms.

Hart, W., Smith, T., 1990. Improved cementing practices reduce cementing failures. J. Can. Pet. Technol. 29 (06), http://dx.doi.org/10.2118/90-06-01s.

Jung, H.B., Jansik, D., Um, W., 2013. Imaging wellbore cement degradation by carbon dioxide under geologic sequestration conditions using X-ray computed microtomography. Environ. Sci. Technol. 47, 283–289. http://dx.doi.org/10.1021/es3012707.

Justnes, H., Skalle, P., Sveen, J., Øye, B.A., 1995. Porosity of oil well cement slurries during setting. Adv. Cement Res. 7, 9–12.

Katende, A., Lu, Y., Bunger, A., Radonjic, M., 2020. Experimental quantification of the effect of oil based drilling fluid contamination on properties of wellbore cement. J. Natural Gas Sci. Eng. 79, 103328. http://dx.doi.org/10.1016/j.jngse.2020.103328.

Kiran, R., Teodoriu, C., Dadmohammadi, Y., Nygaard, R., Wood, D., Mokhtari, M., Salehi, S., 2017. Identification and evaluation of well integrity and causes of failure of well integrity barriers (A review). J. Natural Gas Sci. Eng. 45, 511–526. http://dx.doi.org/10.1016/j.jngse.2017.05.009.

Klinkenberg, L., 1941. The permeability of porous media to liquids and gases. API Drill. Prod. Pract..

Kosmatka, S., Panarese, W., 1988. Design and Control of Concrete Mixtures. Portland Cement Association.

Kumavat, H.R., Chandak, N.R., Patil, I.T., 2021a. Factors influencing the performance of rebound hammer used for non-destructive testing of concrete members: A review. Case Stud. Constr. Mater. 14, e00491. http://dx.doi.org/10.1016/j.cscm.2021.e00491, URL https://www.sciencedirect.com/science/article/pii/S2214509521000061.

Kumavat, H.R., Chandak, N.R., Patil, I.T., 2021b. Influence of wettability on flow characteristics of water through microtubes and cores. Case Studies in Construction Materials 14, e00491. http://dx.doi.org/10.1016/j.cscm.2021.e00491, URL https://www.sciencedirect.com/science/article/pii/S2214509521000061.

Lécolier, E., Rivereau, A., Saoût, G., Audibert-Hayet, A., 2007. Durability of hardened portland cement paste used for oilwell cementing. Oil Gas Sci. Technol. - Rev IFP 62 (3), 335–345. http://dx.doi.org/10.2516/ogst:2007028.

Lesti, M., Tiemeyer, C., Plank, J., 2013. CO2 stability of portland cement based well cementing systems for use on carbon capture & storage (CCS) wells. Cem. Concr. Res. 45, 45–54. http://dx.doi.org/10.1016/j.cemconres.2012.12.001.

Letham, E.A., Bustin, R.M., 2015. Klinkenberg gas slippage measurements as a means for shale pore structure characterization. Geofluids 16 (2), 264–278. http://dx.doi.org/10.1111/gfl.12147.

Li, Z., Liu, H., Guo, X., Ou, H., Gu, T., 2016. Contamination of cement slurries with oil based mud and its components in cementing operations. J. Natural Gas Sci. Eng. 29, 160–168. http://dx.doi.org/10.1016/j.jngse.2016.01.003, URL https://www.sciencedirect.com/science/article/pii/S1875510016300038.

Li, J., Sultan, A.S., 2017. Klinkenberg slippage effect in the permeability computations of shale gas by the pore-scale simulations. J. Natural Gas Sci. Eng. 48, 197–202. http://dx.doi.org/10.1016/j.jngse.2016.07.041.

Lohne, H.P., Ford, E.P., Majourmerd, M.M., Randeberg, E., 2016. Well Integrity Risk Assessment in Geothermal Wells – Status of Today. techreport Delivrable D6.1, IRIS, GeoWell H2020 European Program.

Loosveldt, H., Lafhaj, Z., Skoczylas, F., 2002. Experimental study of gas and liquid permeability of a mortar. Cem. Concr. Res. 32 (9), 1357–1363. http://dx.doi.org/10.1016/S0008-8846(02)00793-7, URL https://www.sciencedirect.com/science/article/pii/S0008884602007937.

Moghadam, A.A., Chalaturnyk, R., 2014. Expansion of the klinkenberg's slippage equation to low permeability porous media. Int. J. Coal Geol. 123, 2–9. http://dx.doi.org/10.1016/j.coal.2013.10.008.

Morris, W., Criado, M.A., Robles, J., Bianchi, G., 2003. Design of high toughness cement for effective long lasting well isolations. In: SPE Latin American and Caribbean Petroleum Engineering Conference. Society of Petroleum Engineers, http://dx.doi.org/10.2118/81001-ms.

Munns, J.W., 1985. The valhall field: A geological overview. Mar. Pet. Geol. 2 (1), 23–43. http://dx.doi.org/10.1016/0264-8172(85)90046-7.

M.W.I.brahim, 1994. Geothermal gradient anomalies of hydrocarbon entrapment, UKCS quadrants 35 to 54. In: Proceedings of European Petroleum Computer Conference. Society of Petroleum Engineers, http://dx.doi.org/10.2118/27547-MS.

Noik, C., Rivereau, A., 1999. Oilwell cement durability. In: SPE Annual Technical Conference and Exhibition. Society of Petroleum Engineers, http://dx.doi.org/10.2118/56538-ms.

Palacio, G.O., Gardner, D., Delabroy, L., Govil, A., 2020. An evaluation of the cement sheath quality of casing sections recovered during a well abandonment operation. In: IADC/SPE International Drilling Conference and Exhibition. Society of Petroleum Engineers, http://dx.doi.org/10.2118/199609-ms.

"Petroleum Safety Authority of Norway Regulations", 2014. The facilities regulations, section 48: well barriers.. URL https://www.ptil.no/en/regulations/all-acts/?forskrift=634.

"Petroleum Safety Authority of Norway Regulations", 2018. The Activities Regulations, Section 85 and 88. Tech. rep., URL https://www.ptil.no/en/regulations/all-acts/?forskrift=613.

Raoof, A., Nick, H., Wolterbeek, T., Spiers, C., 2012. Pore-scale modeling of reactive transport in wellbore cement under CO2 storage conditions. Int. J. Greenhouse Gas Control 11, S67–S77. http://dx.doi.org/10.1016/j.ijggc.2012.09.012.

Ren, Y., Guo, X., Xie, C., Wu, H., 2016. Experimental study on gas slippage of marine shale in southern china. Petrol. J. 2, 171–176. http://dx.doi.org/10.1016/j.petlm.2016.03.003.

Roy-Delage, S.L., Baumgarte, C., Thiercelin, M., Vidick, B., 2000. New cement systems for durable zonal isolation. In: IADC/SPE Drilling Conference. Society of Petroleum Engineers, http://dx.doi.org/10.2118/59132-ms.

Scherer, G.W., Kutchko, B., Thaulow, N., Duguid, A., Mook, B., 2011. Characterization of cement from a well at teapot dome oil field: Implications for geological sequestration. Int. J. Greenhouse Gas Control 5 (1), 115–124. http://dx.doi.org/10.1016/j.ijggc.2010.06.010.

Shadravan, A., Shine, J., 2015. Sustainable zonal isolation under extreme high temperature conditions. In: SPE/IATMI Asia Pacific Oil & Gas Conference and Exhibition. Society of Petroleum Engineers, http://dx.doi.org/10.2118/176301-ms.

Shar, A.M., Mahesar, A.A., Chandio, A.D., Memon, K.R., 2016. Impact of confining stress on permeability of tight gas sands: An experimental study. J. Petrol. Explor. Prod. Technol. 7 (3), 717–726. http://dx.doi.org/10.1007/s13202-016-0296-9.

Shenold, C., Teodoriu, C., 2016. Development of a structured workflow for enhanced well cement integrity: Lessons learned and the way ahead. J. Natural Gas Sci. Eng. 36, 824–836. http://dx.doi.org/10.1016/j.jngse.2016.10.042.

Skadsem, H.J., Gardner, D., Beltrán-Jiménez, K., Govil, A., Palacio, G.O., Delabroy, L., 2021. Study of ultrasonic logs and seepage potential on sandwich sections retrieved from a north sea production well. SPE Drill. Complet.1 -15 http://dx.doi.org/10.2118/206727-PA.

Skadsem, H.J., Gardner, D., Beltrán-Jiménez, K., Kragset, S., Delabroy, L., Ruckert, F., 2020. Fluid migration characterization of cemented sections retrieved from a north sea production well. In: IADC/SPE International Drilling Conference and Exhibition. Society of Petroleum Engineers, http://dx.doi.org/10.2118/199662-ms.

Skadsem, H.J., Kragset, S., Lund, B., Ytrehus, J.D., Taghipour, A., 2019. Annular displacement in a highly inclined irregular wellbore: experimental and three-dimensional numerical simulations. J. Pet. Sci. Eng. 172, 998–1013. http://dx.doi.org/10.1016/j.petrol.2018.09.007.

"Standards Norway", 2013. NORSOk D-010. Well integrity in drilling and well operations. URL https://www.npd.no/globalassets/1-npd/regelverk/skjema/bronnregistreing/eng/norsok-d-010-2013-well-integrity-and-well-operations-rev-4.pdf.

Szilágyi, K., Borosnyói, A., Zsigovics, I., 2014. Extensive statistical analysis of the variability of concrete rebound hardness based on a large database of 60years experience. Constr. Build. Mater. 53, 333–347. http://dx.doi.org/10.1016/j.conbuildmat.2013.11.113, URL https://www.sciencedirect.com/science/article/pii/S095006181301146X.

Tanikawa, W., Shimamoto, T., 2006. Klinkenberg effect for gas permeability and its comparison to water permeabilityfor porous sedimentary rocks. Hydrol. Earth Syst. Sci. Discuss. URL https://www.hydrol-earth-syst-sci-discuss.net/3/1315/2006/hessd-3-1315-2006-print.pdf.

Tanikawa, W., Shimamoto, T., 2009. Comparison of klinkenberg corrected gas permeability and water permeability in sedimentary rocks. Int. J. Rock Mech. Min. Sci. 46 (2), 229–238. http://dx.doi.org/10.1016/j.ijrmms.2008.03.004.

Teodoriu, C., Asamba, P., 2015. Experimental study of salt content effect on class G cement properties with application to well integrity. J. Natural Gas Sci. Eng. 24, 324–329. http://dx.doi.org/10.1016/j.jngse.2015.03.039.

Teodoriu, C., Yuan, Z., Schubert, J., Amani, M., 2012. Experimental measurements of mechanical parameters of class G cement. In: SPE/EAGE European Unconventional Resources Conference and Exhibition. Society of Petroleum Engineers, http://dx.doi.org/10.2118/153007-ms.

Ueda, T., Oki, T., Koyanaka, S., 2018. Experimental analysis of mineral liberation and stereological bias based on X-ray computed tomography and artificial binary particles. Adv. Powder Technol. 29 (3), 462–470. http://dx.doi.org/10.1016/j.apt.2017.11.004.

Vrålstad, T., Todorovic, J., Saasen, A., Godøy, R., 2016. Long-term integrity of well cements at downhole conditions. In: SPE Bergen One Day Seminar. Society of Petroleum Engineers, http://dx.doi.org/10.2118/180058-ms.

Wang, G., Ren, T., Wang, K., Zhou, A., 2014. Improved apparent permeability models of gas flow in coal with klinkenberg effect. Fuel 128, 53–61. http://dx.doi.org/10.1016/j.fuel.2014.02.066, URL https://www.sciencedirect.com/science/article/pii/S0016236114002142.

Wojtanowicz, A., Nishikawa, S., Rong, X., 2001. Diagnosis and Remediation of Sustained Casing Pressure in Wells. Tech. rep., Louisiana State University, URL https://www.bsee.gov/sites/bsee.gov/files/tap-technical-assessment-program/008dk.pdf.

Wolterbeek, T.K., Hangx, S.J., Spiers, C.J., 2016. Effect of CO 2 -induced reactions on the mechanical behaviour of fractured wellbore cement. Geomech. Energy Environ. 7, 26–46. http://dx.doi.org/10.1016/j.gete.2016.02.002.

Xie, S., Shao, J., Burlion, N., 2008. Experimental study of mechanical behaviour of cement paste under compressive stress and chemical degradation. Cem. Concr. Res. 38 (12), 1416–1423. http://dx.doi.org/10.1016/j.cemconres.2008.06.011.

Yang, X., Kuru, E., Gingras, M., Iremonger, S., 2019. CT–CFD integrated investigation into porosity and permeability of neat early-age well cement at downhole condition. Constr. Build. Mater. 205, 73–86. http://dx.doi.org/10.1016/j.conbuildmat.2019.02.004.

Zhou, C., Chen, W., Wang, W., 2015. Evolution of gas permeability for concrete materials under and after uni-axial loading. In: Proceedings of the Second International Conference on Performance-Based and Life-Cycle Structural Engineering. PLSE 2015, School of Civil Engineering, The University of Queensland, http://dx.doi.org/10.14264/uql.2016.754.